



# Non-contact structural displacement measurement using Unmanned Aerial Vehicles and video-based systems

D. Ribeiro<sup>a,\*</sup>, R. Santos<sup>a</sup>, R. Cabral<sup>b</sup>, G. Saramago<sup>c</sup>, P. Montenegro<sup>d</sup>, H. Carvalho<sup>e</sup>, J. Correia<sup>d</sup>, R. Calçada<sup>d</sup>

<sup>a</sup> CONSTRUCT-LESE, School of Engineering, Polytechnic of Porto, Portugal

<sup>b</sup> School of Engineering, Mackenzie Presbyterian University, Brazil

<sup>c</sup> Federal University of Rio de Janeiro, Brazil

<sup>d</sup> CONSTRUCT-LESE, Faculty of Engineering, University of Porto, Portugal

<sup>e</sup> Federal University of Minas Gerais, Brazil

## ARTICLE INFO

### Article history:

Received 15 May 2020

Received in revised form 24 January 2021

Accepted 13 March 2021

### Keywords:

Civil Engineering structure

Displacement

Unmanned Aerial Vehicle

Video system

Inertial Measuring Unit

Validation

## ABSTRACT

This article describes an innovative methodology for estimating in-plane horizontal displacements of Civil Engineering structures based on video systems integrated on Unmanned Aerial Vehicles (UAVs). As the structure and the UAV are both in motion, estimating absolute structural displacements involves, first, assessing the relative displacements of the UAV-structure based on target tracking, and second, subtracting movement of the UAV based on the data derived from an embedded Inertial Measuring Unit (IMU). Computer-vision processing tools based on heuristic features were developed for target tracking, while an efficient numerical integration strategy was implemented for processing IMU data. A successful integration process requires a baseline correction of the records through the application of high-pass filters and a rigorous control of distortion errors. The validation of the proposed methodology was based on exploratory dynamic tests performed in the laboratory and in the field.

The laboratory test involved measuring the displacements of a moving target, positioned over a seismic table using a Linear Variable Differential Transformer (LVDT), a DC accelerometer and the UAV video system in a stationary position. An excellent agreement was achieved for the three estimated displacements, both in the time and frequency domains. In particular, the comparison between the video and the LVDT displacement records showed a peak value error of 0.096 mm and a Root Mean Square (RMS) error of 3.1%.

The field test consisted of measuring the displacements of a target fixed to a massive Reinforced Concrete (RC) wall based on the UAV video system in motion. Under these circumstances, the target does not experience any movement, and therefore, the virtual displacement of the target estimated by the video is due exclusively to the self-movements of the UAV. The comparison between the video and the IMU displacement records shows a good agreement, with a peak value error of 1.47 mm (15.5% relative error) and a RMS error of 9.3%.

The results of this study are a step forward in estimating the absolute displacements of a vibrating structure based on camera-based measurement from UAVs, specifically with the support of IMU systems for the elimination of measurement inaccuracies as a result of the UAV motion.

© 2021 Elsevier Ltd. All rights reserved.

\* Corresponding author.

E-mail address: [drr@isep.ipp.pt](mailto:drr@isep.ipp.pt) (D. Ribeiro).

## 1. Introduction

The general assessment of civil engineering assets is an important instrument for infrastructure managers to evaluate their structural integrity and operability and to estimate possible maintenance or rehabilitation needs. In specific situations, the condition assessment is performed based on information obtained from Structural Health Monitoring (SHM) systems [1]. These systems comprise a wide range of sensors capable of measuring the effects of operational and environmental loads, typically displacements, velocities and accelerations.

Displacement measurements have been particularly relevant for modal identification [2], structural damage identification [3] and structural safety assessment [4,5], among others, and can be obtained using contact [6] or non-contact systems [7,8]. The contact systems generally encompass high precision displacement transducers, such as LVDTs and cable transducers. The main disadvantage of LVDTs is their dependence on a fixed reference point, which, in many cases, can be difficult or even impossible to materialize, e.g., in structures located over a watercourse, a road or a rugged terrain. Non-contact measurement systems rely on technologies based on laser [9], radar [10], GPS [11] and on the processing and analysis of images obtained by video [12,13] or digital photography [14]. Non-contact systems have evident advantages as they do not require a fixed reference point, therefore, there is no need to access the measured structures, which significantly reduces installation time. However, new technological challenges are arising, especially, the increase of the measurements' accuracy for larger distances, the enhance of performance on dynamic measurements and under adverse environmental conditions, and the integration on passing vehicles [15,16].

In recent years, computer vision-based methods have become viable alternatives for measuring structural displacements in SHM systems [17]. Computer vision mainly uses two types of tracking methods, the target [7,15] and the non-target methods [17,18]. Target methods are based on the tracking of reference points of artificial targets, e.g., transition points between different colored regions, centroids of specific colored regions, etc., and typically require the application of heuristic image processing techniques based on edge detectors and morphological operators [19]. Conversely, non-target methods are usually based on Digital Image Correlation techniques, consisting in the tracking of specific feature points from the images that keep invariant properties during an event, and typically require a higher computational effort [20].

More recently, some applications of vision-based displacement systems mounted on Unmanned Aerial Vehicles (UAVs) have been developed and tested in the laboratory and in the field [2,21–25]. The use of UAVs has several advantages, namely [26,27]: *i*) the possibility of positioning the video system in a line-of-sight appropriate to the monitored structure, avoiding perspective distortions and easily accessing remote locations in potentially hazardous conditions, *ii*) capturing images at lower distances with greater accuracy regarding image-processing, and *iii*) as the UAV can move closer to the structure, atmospheric effects are reduced. In contrast to the measurements using a fixed reference point, however, the UAV is a non-stationary reference point and, therefore, its movements considerably affect the measured displacements of the structure [22]. Changing from a stationary to a non-stationary measuring point poses a major challenge for the signal analysis, particularly in what concerns the development of methods to measure the absolute displacement of the structure instead of the structure-camera relative displacement. Thus, in order to increase the accuracy of the absolute displacement estimate, several camera motion subtraction techniques have been developed, namely: *i*) using digital high-pass filtering [2,24], *ii*) using a stationary background object [15,21,23], and *iii*) using an Inertial Measuring Unit (IMU) [25,28].

The first approach is based on the application of digital high-pass filtering to the camera's displacement records, and relies on the assumption that the UAV motion, considering the current GPS stabilization, occurs predominantly at frequencies below 0.5 Hz, and the movements of the structure occur mainly at higher frequencies. Garg et al. [24] conducted an outdoor test in which a Laser Doppler Vibrometer (LDV) mounted on a UAV was used to collect displacement measurements of a moving target structure. The UAV was connected to the ground by a rope, which distorted its dynamic response, despite allowing a more effective uncoupling of the dynamic behaviour of the UAV from the dynamic behaviour of the structure. The results showed that the signal difference between the measured dynamic data from the moving LDV and a LVDT was less than 5% in peak values and 10% in the relative error of the RMS. However, a detailed comparison between both records showed distinct levels of accuracy over time. The influence of the very-low-frequency movements of the UAV was removed using a high-pass Butterworth filter of order 3 and a cutoff frequency of 0.5 Hz. Nevertheless, a high-pass filtering approach significantly limits the ability to estimate the absolute displacements of the structure, and the assessment of displacements in structures with very low natural frequencies.

In the second approach, the motion of the camera is estimated based on features extracted from stationary background objects, e.g., buildings, rocks, tree trunks and manually installed markers. These objects are normally located close to the measured structure, which, in some real-world applications, may not be easy to identify. The absolute displacement of the structure can be obtained based on the information of the UAV motion and the relative displacement measured between the structure and the camera. Yoon et al. [23] stress that this background motion is a 2D projection of the 3D motion of the camera, which includes translation and rotation movements. Zhang et al. [15] conducted laboratory tests to evaluate the structural displacements on an artificial target subjected to increasing static movements, up to 50 mm. Considering the UAV at a 9.75 m operating distance from the monitored structure, the system achieves an average RMS error of 5.12% (less than 0.5 mm error in absolute value) based on the results of six distinct tests, in comparison to the results provided by a LVDT. Ellenberg et al. [21] performed laboratory tests to evaluate the vertical displacements in reduced-scale models of a

cantilever beam and a steel bridge deck under static loadings. The UAV images were obtained for two distinct configurations, stationary and while hovering, and the results showed that the UAV had an accuracy of  $\pm 2.0$  mm in a stationary configuration, and an accuracy of  $\pm 3.5$  mm while hovering, comparable to an optical precision system. The existing studies using stationary background objects for UAV motion correction are mainly based on indoor laboratorial experiments, and no outdoor experiments were identified. Additionally, the tests were essentially conducted under static loadings and few tests were performed under dynamic loadings.

Finally, in the third approach, the estimation of the UAV motion is based on data provided by an IMU, which consists of a set of DC type gyroscopes and accelerometers capable of responding to very low frequency movements (virtually 0 Hz). Precise estimations of the displacements and rotations of the UAV are obtained by the double integration of acceleration measurements or by the simple integration of angular velocities, respectively. Typically, the integration procedure is affected by errors that cause distortions in the baseline signal (drift), which are amplified in the case of double integration [29]. Errors are generally caused by limitations of A/D conversion, external noise sources and baseline errors due to the unknown initial conditions of the movement [30,31]. Thus, the success of the integration process requires a baseline adjustment of the signals by applying high-pass filters or using linear, bilinear or polynomial corrective functions [32]. High-pass filters not only remove the baseline errors but also eliminate the low-frequency content of the signal associated with quasi-static movements. To prevent low-frequency noise after high-pass filtering, Arias-Lara & De la Colina [32] suggest the addition of segments of zeros at the beginning and end of the acceleration record. For the estimation of the absolute displacements of the UAV, Herrmann et al. [25] suggest a data fusion procedure based on data from GPS and accelerometers, in which the GPS captures the very low frequency movements of the UAV and the double integration of the accelerations captures the higher frequency movements of the UAV. No practical applications were identified in the consulted bibliography about the use of IMUs in the estimation of self-displacements of the UAV. The applications found are mainly related to position tracking of UAVs in large-scale navigation problems [28,33]. Thus, this study aims at giving clear and effective contributions regarding some aspects that are not sufficiently addressed in the existing bibliography.

First, the development of a non-contact methodology based on UAVs equipped with video cameras for evaluating the displacements of Civil Engineering structures and specifically focused on the in-plane horizontal movements. This type of displacement has been regularly used as a key performance indicator for assessing the safety and serviceability of bridges where the transverse displacement is a concern [4], buildings [34] and telecommunication towers [5]. Second, the development of an innovative UAV motion subtraction technique based on an embedded inertial system capable of characterizing the UAV movements for very low frequencies, down to 0.10 Hz. This strategy is a step forward on the estimation of the absolute displacements of the structure, which, in the existing bibliography, were not possible to obtain, since high-pass filters were used to remove the influence of low frequency movements of the UAV [2,24]. Third, conducting a detailed study on numerical integration techniques of the acceleration signals, namely the one based on the application of high-pass digital filters. This study will provide clear conclusions about the truncation periods that should be applied to the displacement signals in order to avoid the distortion errors and obtain reliable results. Finally, validating the UAV motion subtraction technique based on an outdoor dynamic test and proving its efficiency and robustness in a wide range of frequencies, including very-low frequencies.

## 2. Methodology for displacement measurement using UAVs and inertial systems

### 2.1. Concept

The proposed methodology for measuring non-contact displacements is based on the tracking of a target fixed to the structure using a video system and a UAV, also known as drone, without a fixed reference point (Fig. 1). As the structure and the UAV are both in motion, the tracking of the target allows obtaining the relative displacements between the structure and the UAV. It is, therefore, necessary to evaluate and compensate the movements of the drone in order to obtain the absolute displacements of the structure. The target tracking is carried out based on the application of advanced image processing techniques that allow the precise determination of the target position in each frame of the video (Section 3.1). The compensation of the drone's movements is performed based on the data recorded in an internal Inertial Measurement Unit (IMU) composed of accelerometers and gyroscopes. Based on the acceleration records of the accelerometers and the angular velocity records of the gyroscopes, it is possible to estimate the displacements and rotations of the UAV using numerical integration techniques (Section 3.2).

In addition, the movements of the UAV are corrected by means of a position correction system of the type Real Time Kinematic (RTK) with the support of a local station. The local station has a precision geodesic GPS that calculates and records the coordinates of its position, serving as a stationary geographic reference for the UAV that is in motion. During the flight, the UAV's high-precision GPS sensor exchanges information with satellites and the local station in order to correct the geographic position of the UAV, considering the fixed point recorded by the station. The RTK system allows the UAV movements to be limited to  $\pm 1.0$  cm in the horizontal direction and  $\pm 1.5$  cm in the vertical direction.

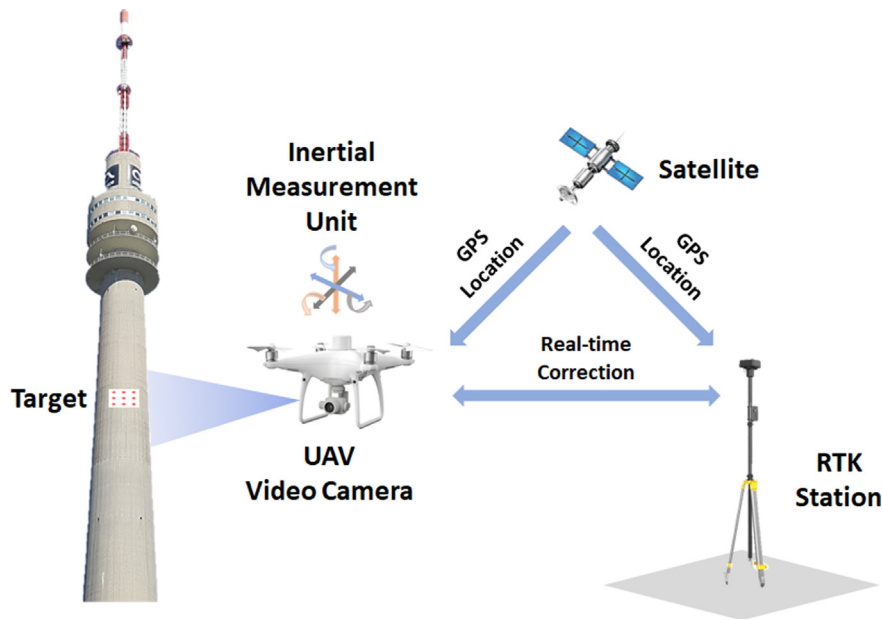


Fig. 1. Non-contact displacement measurement system using a UAV and a video system.

## 2.2. Components

The components of the non-contact displacement measurement system, including its main technical characteristics, are shown in Fig. 2. The UAV is from DJI, model Phantom 4 RTK, with a maximum load equal to 1.39 kg, a maximum velocity of 50 km/h and a flight range of approximately 28 min. The drone has an internal inertial measurement system that includes a triaxial accelerometer, three uniaxial gyroscopes, a magnetometer, an altimeter and a barometer. In addition, the UAV has an RTK position correction system working in conjunction with the local D-RTK 2 station that contains a precision geodesic GPS

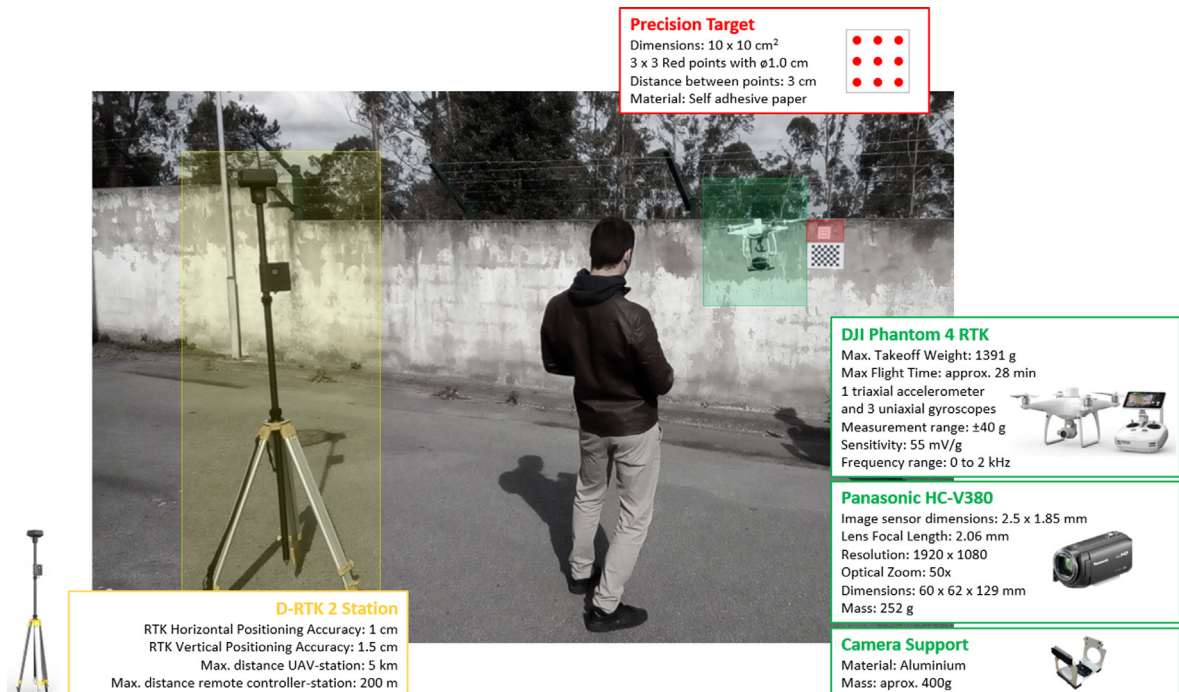


Fig. 2. Technical characteristics of the main components of the displacement measurement system.

and serves as a stationary reference for the aircraft. The drone also has a native camera mounted on a suspension / pivot system, called a gimbal, with internal stabilizers that cannot be disabled. Therefore, relative movements occur between the native camera and the body of the UAV, where the inertial system is located, which makes the movements recorded by the native camera different from the actual movements of the drone. To overcome this problem, and after analyzing several alternative solutions, it was convenient to attach an additional external camera to the drone, rigidly connected to the body of the UAV.

The external video camera is from Panasonic, model HC-V380, and has a maximum video resolution of 2.2MP (1920 × 1080), an acquisition frequency of 60 fps at maximum resolution, a 50× optical zoom and a mass of 252 g. During the operation of the camera, the image stabilizer is deactivated, and the transmission of the images is carried out remotely to a smartphone using the Wi-Fi protocol. The data is stored using a memory card. The camera is mounted on an aluminium support attached to the body of the UAV with PVC clamps. The camera support mass must be minimized in order to avoid compromising the UAV stability and flight safety if over 700–800 g. However, it must be of a certain minimum mass in order to maintain the level of rigidity required for acceptable performance. 400 g was achieved in this case.

The precision target consists of a set of nine red circles, with a diameter equal to 1.0 cm, arranged in an orthogonal grid with spacing equal to 3.0 cm, and resting on a white square base measuring 10 cm on each side.

### 2.3. Mathematical formulation

This study focuses specifically on the estimation of the absolute displacements of the structure in its plane and in the direction of Y axis (according to Fig. 3). The absolute displacement of the structure in this direction ( $\vec{\delta}_s^{Y,i}$ ) is determined based on the vector sum of the displacement of the target obtained by processing the video images ( $\vec{\delta}_v^{Y,i}$ ), as detailed in Section 3.1, compensated by the displacement of the UAV ( $\vec{\delta}_{UAV}^{Y,i}$ ), for each time step  $i$ :

$$\vec{\delta}_s^{Y,i} = \vec{\delta}_v^{Y,i} + \vec{\delta}_{UAV}^{Y,i} \quad (1)$$

The degrees of freedom representing the movements of the UAV are illustrated in Fig. 3 and refer to the geometric centre of the inertial system: three displacements, according to axes X, Y and Z, and three rotations,  $\alpha$ ,  $\beta$  and  $\gamma$ , around axis X, Y and Z, respectively. The X axis is perpendicular to the motion plane (target).

The value of the virtual displacement of the target in the direction of axis Y due to the movements of the UAV ( $\delta_{UAV}^{Y,i}$ ) can be determined from the sum of four terms of the UAV movement:

$$\delta_{UAV}^{Y,i} = \delta_Y^{Y,i} + \delta_X^{Y,i} + \delta_\alpha^{Y,i} + \delta_\gamma^{Y,i} \quad (2)$$

where  $\delta_Y^{Y,i}$  is the term resulting from the movement of the UAV in the direction Y,  $\delta_X^{Y,i}$  is the term resulting from the movement of the UAV in the direction of axis X, whose approximation or distance to the target indirectly induces a virtual movement of the target in the direction Y,  $\delta_\alpha^{Y,i}$  is the term resulting from the rotation of the UAV around axis X, which, due to the fact that the inertial system is distanced from the video system, induces a virtual displacement of the target in the direction Y, and  $\delta_\gamma^{Y,i}$  is the term resulting from the rotation of the UAV around axis Z, that also induces a virtual displacement of the target in the direction Y, where all terms refer to time step  $i$ .

The estimation of  $\delta_Y^{Y,i}$  must consider the three-dimensional movement of the UAV, in which the translation component in the direction of axis Y is influenced by the translation components in the direction of axes X and Y, due to the existence of rotations around the various axes. Thus, the acceleration records corrected for the rotational effect  $a'_X(t)$ ,  $a'_Y(t)$ ,  $a'_Z(t)$  according to axes X, Y and Z, respectively, can be obtained from the corresponding non-corrected accelerations,  $a_X(t)$ ,  $a_Y(t)$ ,  $a_Z(t)$ , through the following expression:

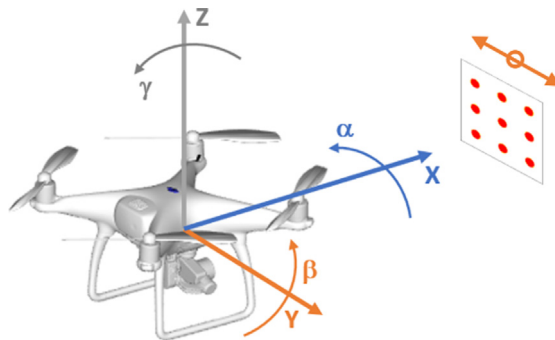


Fig. 3. Reference degrees of freedom characterizing the movement of the UAV and direction of the target motion.



$$\begin{bmatrix} a'_x(t) \\ a'_y(t) \\ a'_z(t) \end{bmatrix} = \begin{bmatrix} \cos\alpha\cos\beta & \cos\alpha\sin\beta\sin\gamma - \sin\alpha\cos\gamma & \cos\alpha\sin\beta\cos\gamma + \sin\alpha\sin\gamma \\ \sin\alpha\cos\beta & \sin\alpha\sin\beta\sin\gamma + \cos\alpha\cos\gamma & \sin\alpha\sin\beta\cos\gamma - \cos\alpha\sin\gamma \\ -\sin\beta & \cos\beta\sin\gamma & \cos\beta\cos\gamma \end{bmatrix} \cdot \begin{bmatrix} a_x(t) \\ a_y(t) \\ a_z(t) \end{bmatrix} \quad (3)$$

where  $\delta_Y^{Y,i}$  is determined by the double integration of the acceleration records in the direction of axis Y corrected for the rotational effect  $a'_y(t)$ , according to the following expression (Fig. 4a):

$$\delta_Y^{Y,i} = \iint_{t_{i-1}}^{t_i} a'_y(t) \cdot dt \cdot dt \quad (4)$$

In addition to the term in Equation (4), if the target is not centred in relation to axis X, the movement of approximation/distance of the UAV in relation to the target (scaling) results in a virtual displacement of the target in the direction of axis Y ( $\delta_X^{Y,i}$ ), which can be obtained through the following relation (Fig. 4b):

$$\delta_X^{Y,i} = (D_{i-1} - D_i) \cdot \frac{Q_{i-1}}{D_{i-1}} = \iint_{t_{i-1}}^{t_i} a'_x(t) \cdot dt \cdot dt \cdot \frac{Q_{i-1}}{D_{i-1}} \quad (5)$$

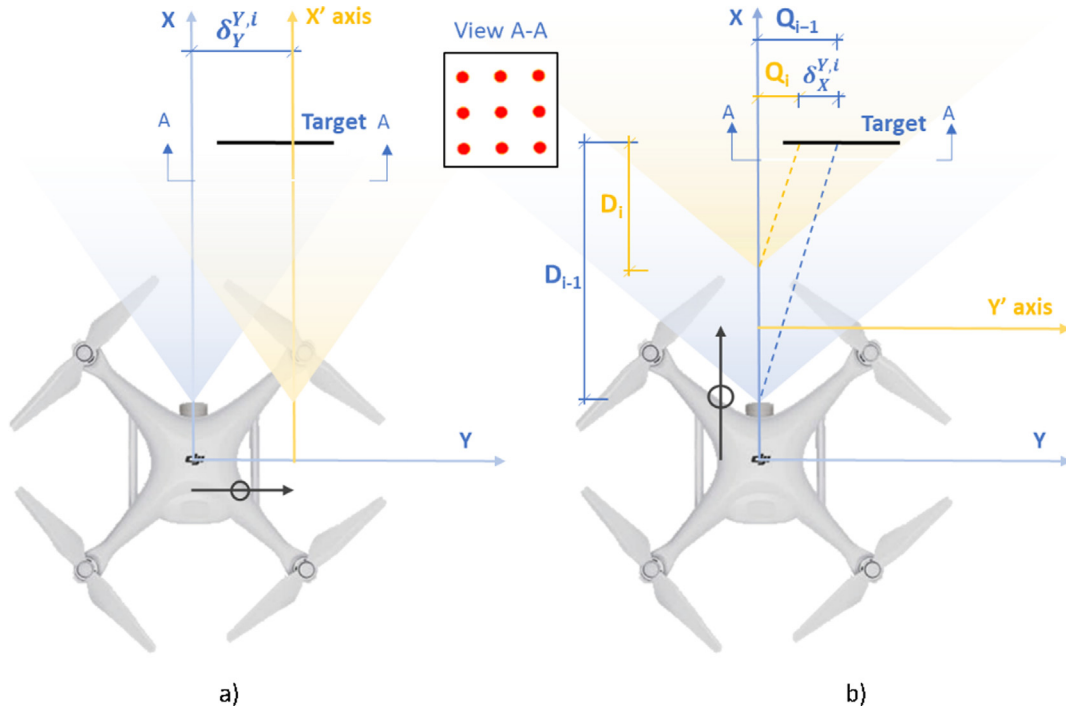
where  $D_{i-1}$  and  $D_i$  are distances from the drone to the target measured in the direction of axis X for the time steps  $i-1$  and  $i$ , respectively, and  $Q_i$ ,  $Q_{i-1}$  are the distances from the centre of the camera sensor to the centre of the target, measured in the direction of axis Y for the time steps  $i$  and  $i-1$ , respectively.

Fig. 5a and b present the virtual displacements of the target due to the rotations of the UAV around axes X and Z, respectively. These displacements are estimated based on the simple numerical integration of the angular velocity records obtained by the gyroscopes, in order to find the corresponding rotations, and by applying the following expressions:

$$\delta_\alpha^{Y,i} = C \cdot \int_{t_{i-1}}^{t_i} \dot{\alpha}(t) \cdot dt \quad (6)$$

$$\delta_\gamma^{Y,i} = D_i \cdot \int_{t_{i-1}}^{t_i} \dot{\gamma}(t) \cdot dt \quad (7)$$

where  $C$  is the distance from the gyroscope to the video camera sensor,  $D_i$  is the distance from the UAV to the target along axis X, and  $\alpha$ ,  $\gamma$  are the rotations around axes X and Z, respectively.



**Fig. 4.** Virtual displacements of the target in the direction of axis Y due to the movement of the UAV in the direction of axes: a) Y ( $\delta_Y^{Y,i}$ ), b) X ( $\delta_X^{Y,i}$ ) (both plan views).

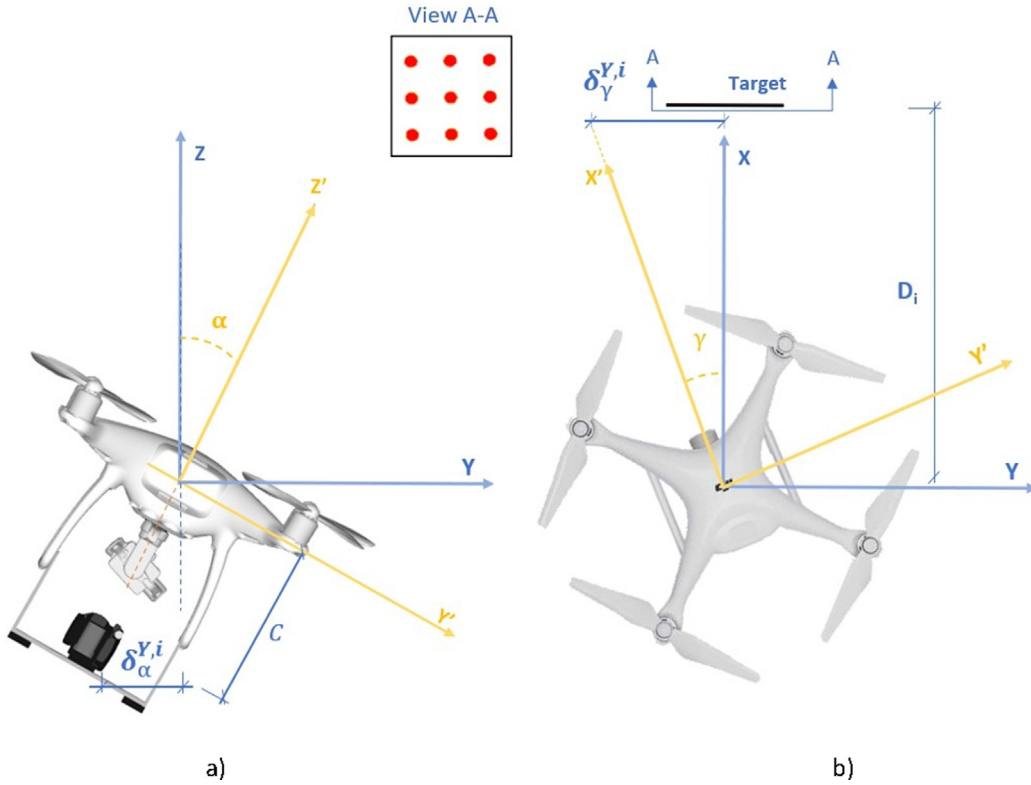


**Fig. 5.** Virtual displacements of the target in the direction of axis Y due to the rotation of the UAV around axes: a) X ( $\delta_\alpha^{Y,i}$ ) (lateral view), b) Z ( $\delta_\gamma^{Y,i}$ ) (plan view).

The distance  $D_i$  between the video camera sensor and the target, for the initial time step (0 s), can be estimated through the elementary principle of optics illustrated in Fig. 6, assuming the camera sensor plan parallel to the target plane. Based on this figure, it is possible to verify that if the focal distance ( $f$ ), the horizontal dimension of the video camera sensor ( $h$ ) and the horizontal dimension of the field of vision ( $H_i$ ) are known, distance  $D_i$  can be calculated through the following expression:

$$D_i = \frac{f}{h} \cdot H_i \quad (8)$$

The focal distance and the dimensions of the video camera sensor are typically provided by the manufacturer (Fig. 2). The horizontal dimension of the field of vision at time step  $i$  can be estimated based on the following expression:

$$H_i = n_{px,h} \cdot r^i \quad (9)$$

where  $n_{px,h}$  is the number of pixels of the video camera sensor in the horizontal dimension and  $r^i$  is the image resolution (Section 3.1).

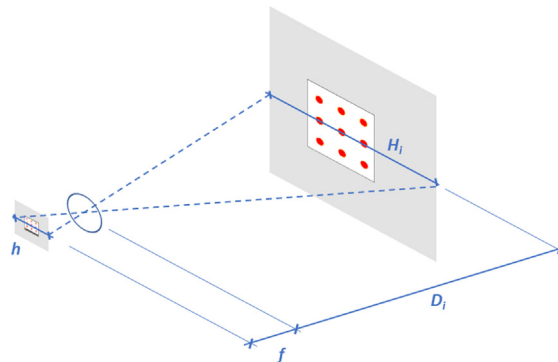


**Fig. 6.** Determination of distance  $D_i$  between the video camera sensor and the target, for the initial time step (0 s).

Therefore, rewriting the Eq. (2), the value of the virtual displacement of the target in the direction of axis Y due to the movement of the drone, at each time step  $i$ , will be counted through the following expression:

$$\delta_{UAV}^{Y,i} = \iint_{t_{i-1}}^{t_i} a'_Y(t) \cdot dt \cdot dt + \iint_{t_{i-1}}^{t_i} a'_X(t) \cdot dt \cdot dt \cdot \frac{Q_{i-1}}{D_{i-1}} + C \cdot \int_{t_{i-1}}^{t_i} \dot{\alpha}(t) \cdot dt + D_i \cdot \int_{t_{i-1}}^{t_i} \dot{\gamma}(t) \cdot dt \quad (10)$$

### 3. Heuristic image processing and numerical integration tools

The non-contact displacement measurement methodology involved the development of two computational tools, one for the heuristic processing of video images and the other for the numerical integration of the signals from the inertial system, both developed in the Matlab software (Fig. 7). The video image processing tool aims at estimating the relative displacements between the UAV and the target fixed to the structure. The numerical integration tool, in turn, allows estimating the movements of the UAV, in particular the displacements and rotations, based on the records from the internal inertial system. Using both tools, an estimate of the absolute displacement of the structure is obtained from the displacements of the video tracking corrected by the movements of the UAV.

#### 3.1. Heuristic processing of video images

The target tracking methodology is based on the application of morphological operators, particularly on segmentation, which involves the division of each image into regions (sets of pixels) that are similar in a given property, in this case colour. Fig. 8 shows the ordered sequence of the morphological operators that constitute the image tracking algorithm, with a graphical representation of the effect of its application.

The original RGB image is subjected to a segmentation operation that allowed to separate the background from the red circles of the target. For this purpose, the G and B channels were subtracted from the image and the image was converted to the grayscale.

The resulting image is then converted to a binary image, in black and white. In this step, a filter is also applied to eliminate clusters of white pixels from areas of the image other than the circular areas of the target. The maximum number of pixels that constitute these clusters is empirically defined by the user, usually between 100 and 300 pixels, according to the lighting conditions and the distance from the camera to the target.

Subsequently, based on the binary image, the coordinates (x, y) of the centroid of the nine circular areas of the target are determined, in pixels. The origin of the referential (x, y) is considered in the upper left corner of the field of vision. In the end, for better visualization, the tracking of the binary image is overlaid with the original image.

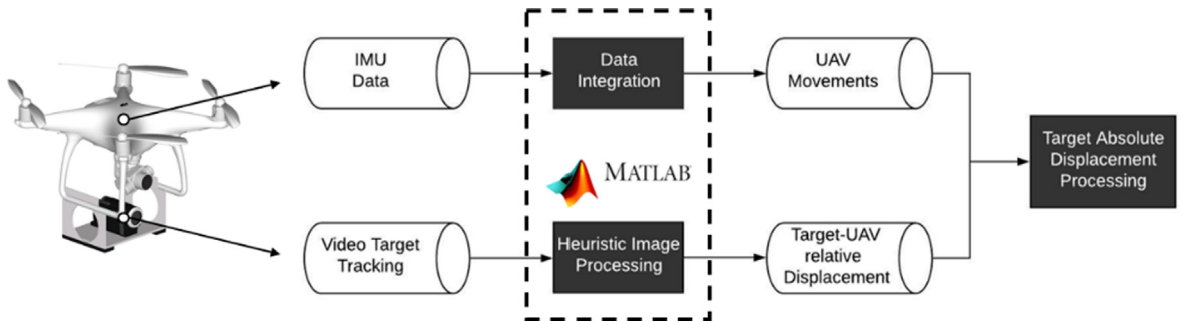


Fig. 7. Workflow of the heuristic image processing and numerical integration tools.

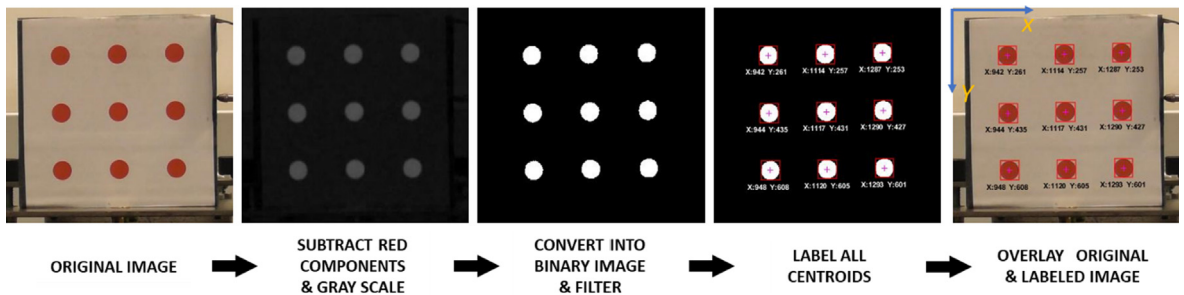


Fig. 8. Heuristic image processing for target tracking.



Image resolution is calculated for each pair of circular areas at time step  $i$  ( $r_j^i$ ), in px/mm, for a total of 6 values ( $r_1^i$  to  $r_6^i$ ) in the direction of axis X, based on the following expressions and the indications in Fig. 9:

$$r_j^i = \frac{X_{j+3}^i - X_j^i}{\left[30 \cdot \cos \gamma_i \cdot (1 - \sin^2 \alpha_i)\right]} \quad j = 1 \text{ to } 6 \quad (11)$$

where  $X_j^i$  is the coordinates of axis X of the centroid of circular area  $j$ , in pixels, at time step  $i$ , and  $\alpha_i$ ,  $\gamma_i$  are the rotations of the UAV-video system, at time step  $i$ , in relation to axis X and Z, respectively, given by:

$$\alpha_i = \int_{t_{i-1}}^{t_i} \dot{\alpha}(t) \cdot dt \quad (12)$$

$$\gamma_i = \int_{t_{i-1}}^{t_i} \dot{\gamma}(t) \cdot dt \quad (13)$$

The numbering of the circular areas is shown in Fig. 8 and the distance between them is equal to 30 mm. Based on the 6 singular values of the image resolution, the  $n$  individual values ( $n < 6$ ) greater than 3 times the Mean Absolute Deviation (MAD) are discarded. The Mean Absolute Deviation at time step  $i$  is given by:

$$MAD^i = \frac{\sum_{j=1}^6 |r_j^i - \bar{r}^i|}{6} \quad (14)$$

where  $\bar{r}^i$  is the mean image resolution at time step  $i$ . Thus, the image resolution at time step  $i$  ( $r^i$ ), in px/mm, which is variable in time due to the movement of the camera in the direction of the target and due to the perspective distortion, is given by:

$$r^i = \frac{\sum_{j=1}^n r_j^i}{n} \quad (15)$$

When the image resolution is known, the value of the horizontal displacement of the target at time step  $i$  ( $\delta_V^{y,i}$ ) is obtained through the following expression:

$$\delta_V^{y,i} = \delta_V^{y,i-1} + \left[ \frac{\left( \sum_{j=1}^9 X_j^i - X_j^{i-1} \right)}{9} \times \frac{1}{r^i} \right] \quad (16)$$

The image distortion errors, essentially due to barrel and pincushion distortions, were neglected due to the following reasons: i) the video camera is equipped with very low distortion lens [35], as proved in preliminary laboratory tests with a dedicated calibration target, where maximum errors on the order of 0.03 mm – primarily occurring on the lateral sides of the images – were obtained [36]; and, ii) the positioning of the target within the central region of the image – where the image distortion is at a minimum [37].

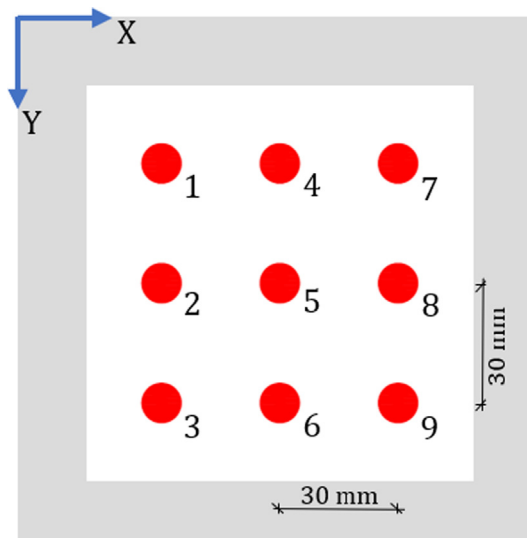


Fig. 9. Referential for image tracking.

### 3.2. Numerical integration tool

#### 3.2.1. General aspects

Fig. 10 illustrates the ordered sequence of the signal processing operations included in the numerical integration algorithm, with a graphical representation of the effect of its application.

The algorithm is based on the sequential application of two operators, one with numerical integration and the other with a high-pass digital filter, and allows the execution of single or double integration.

The numerical integration was performed using the Trapezoidal Rule. This integration technique is presented in the following expression, in which the system is at rest, or assumed to be at rest, in the initial time step:

$$\begin{cases} f(t_0) = 0 \\ \int_a^b f(t)dt \cong \sum_{i=0}^{n-1} \left[ \frac{f(t_{i+1}) + f(t_i)}{2} \right] \cdot \Delta t_i \end{cases} \quad (17)$$

where  $f(t)$  is the original record,  $[a, b]$  is the interval of the numerical integration,  $n$  is the number of samples and  $\Delta t_i$  is the time interval between  $t_i$  and  $t_{i+1}$ , generally equal to the time between signal samples.

The high-pass filter used after each numerical integration is a Finite Impulse Response based on Kaiser's window (FIR-Kaiser type) with a variable cutoff frequency, usually between 0.10 Hz and 0.50 Hz, a pass band attenuation of 0.01 dB and a stop band attenuation of 20 dB. This filter allows removing the errors generated in the numerical integration at low frequencies, acting specifically in the removal of the constant component resulting from each integration.

As the use of filters causes a time lag in the signal, the digital filtering process is typically carried out in two directions: a filter applied directly to the original signal, followed by a filter applied to the resulting reversed signal, which results in a zero-time lag of the signal.

It should be noted that the use of high-pass filters to correct the signal after the numerical integration creates distortions at the beginning of the record. When using double filters, these distortions may also occur at the end of the record, which is why these two parts of the record should be disregarded. The effect of signal distortions is clearly visible in the velocity and displacement records presented as an example in Fig. 10.

#### 3.2.2. Signal distortion effect

This section aims at identifying which parts of the records were affected by the distortion errors derived from the integration process, particularly from the application of high-pass filters, and therefore must be removed. For this purpose, it is considered an input signal in accelerations,  $a(t)$ , of the sinusoidal type, with amplitude  $A$  and angular frequency  $\omega (= 2\pi f)$ :

$$a(t) = A \cdot \sin(\omega t) \quad (18)$$

In these circumstances, the expressions characterizing the signals of velocity,  $v(t)$ , and displacement,  $d(t)$ , are known, by application of a simple and double integration procedure, respectively.

The application of the numerical integration tool also allows estimating the records of velocities,  $v(t)$ , and displacements,  $d(t)$ . The difference between the values obtained analytically and through the numerical integration,  $\varepsilon(t)$ , results from the distortion errors of the signals in terms of velocity,  $\varepsilon_v(t)$ , and displacement,  $\varepsilon_d(t)$ .

Fig. 11a illustrates the comparison between the velocity and displacement records obtained analytically and through the numerical integration, considering  $A = 1 \text{ m/s}^2$  and  $f = 1 \text{ Hz}$ , and applying a high-pass FIR-Kaiser filter with a cutoff frequency

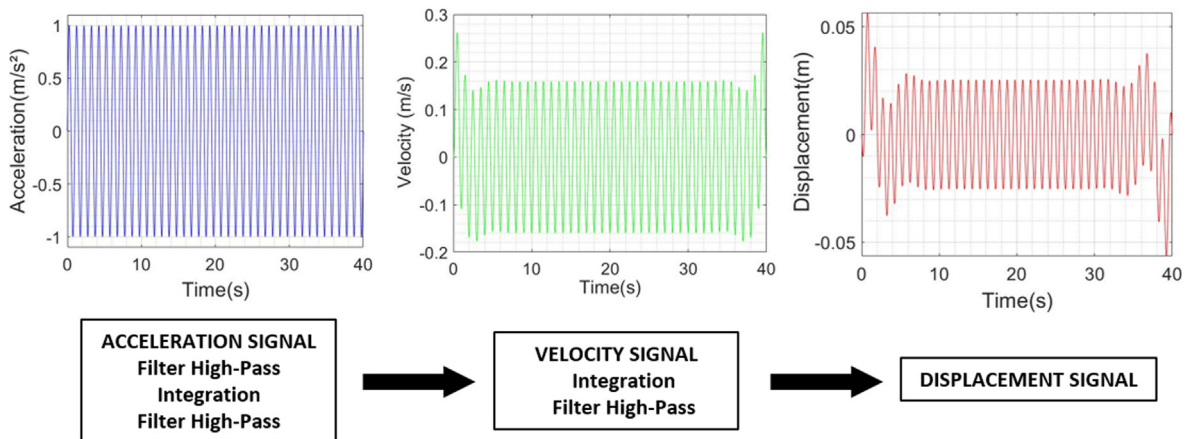
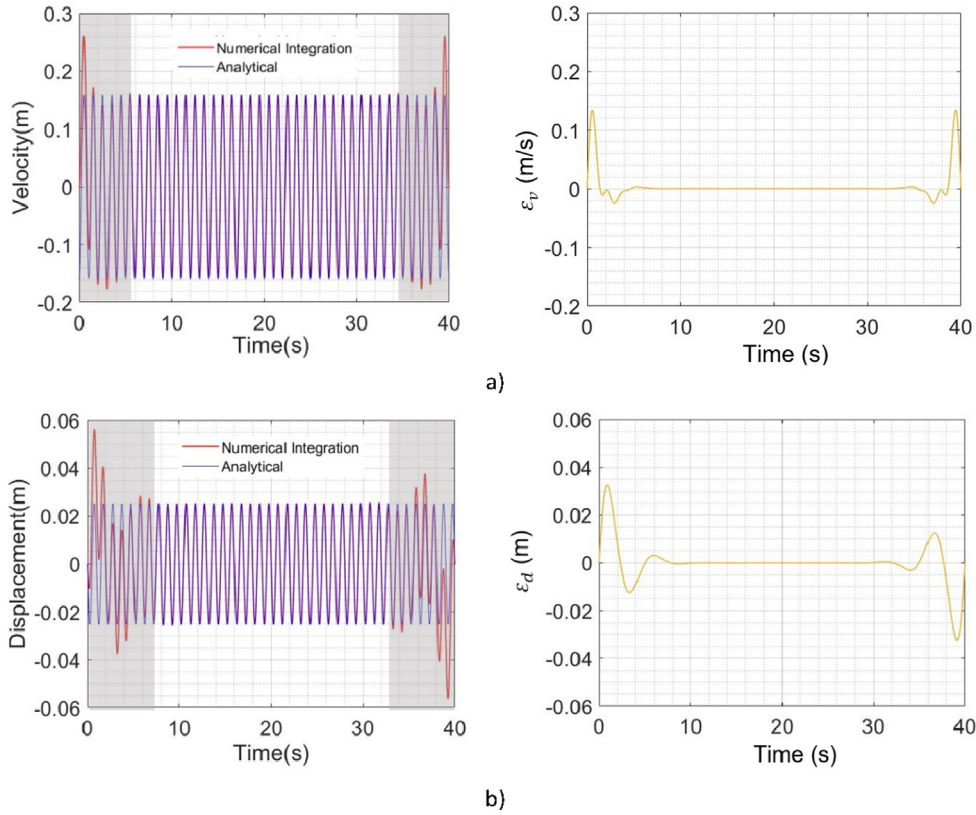


Fig. 10. Signal numerical integration tool.



**Fig. 11.** Comparison of the records obtained analytically and through the numerical integration, and their respective relative errors: a) velocities, b) displacements.

equal to 0.30 Hz. The shaded time intervals are those in which the distortion effect of the signal obtained through the numerical integration is visible. The error functions associated with velocity,  $\varepsilon_v$ , and displacement,  $\varepsilon_d$ , records are also shown.

The results illustrate the distortion effect of the records obtained by numerical integration, a situation that is more visible in the case of displacements, due to the double application of the high-pass filter. Regarding the displacement records, the greatest differences between the results obtained analytically and through the numerical integration occur in the time intervals [0–6]s and [34–40]s, which coincide with the beginning and end parts of the record, respectively. With the exception of these time intervals, there is a perfect agreement between the records obtained analytically and through the numerical integration.

Fig. 12 illustrates how the variation of the cutoff frequency values of the high-pass filters (0.10 Hz, 0.30 Hz and 0.50 Hz) influences the distortion of the displacement records. Fig. 12a presents the functions of the high-pass filters and Fig. 12b shows the error functions associated with the displacement records,  $\varepsilon_d$ . The results of the analysis show that the lower the cutoff frequency, the longer the duration of the distortion. It should be noted that the use of a high-pass filter with a cutoff frequency equal to 0.10 Hz causes a distortion in the displacement record for a time length of 60 s, 30 s at the beginning and 30 s at the end, which corresponds to 50% of the total duration of the record.

#### 4. Validation of the methodology based on experimental tests

The displacement measurement methodology and the computational tools for image processing and numerical integration were validated based on two exploratory experimental tests, one performed in the laboratory and the other in the field.

##### 4.1. Laboratory test

The laboratory test consisted of measuring the horizontal displacements of a moving target, positioned on a seismic table, with the help of non-contact and contact measurement systems (Fig. 13).

The non-contact measurement system involved two different components: the video system and a DC accelerometer, PCB model 3741B1210G. The video system was positioned over a rigid table, about 1.5 m from the target, and coupled to the UAV in stationary position. The camera was adjusted to capture images in high resolution format (1920 × 1080) and an acquisi-

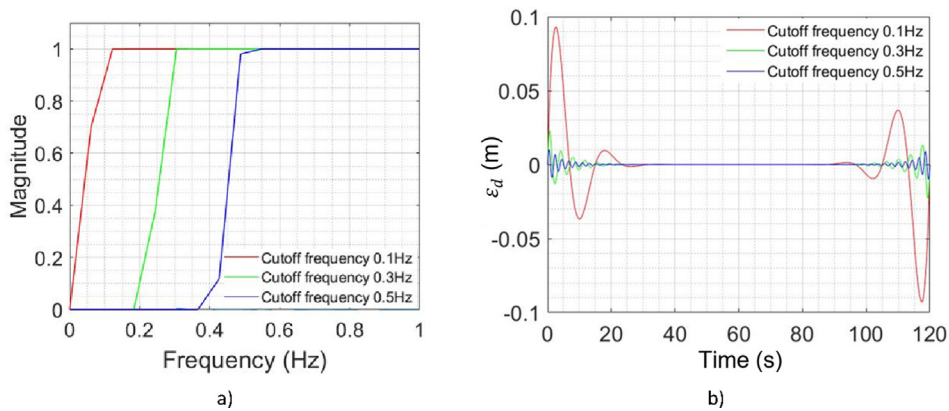


**Fig. 12.** Influence of the filter cutoff frequency on the distortion of the displacement record: a) filter functions, b) error functions.

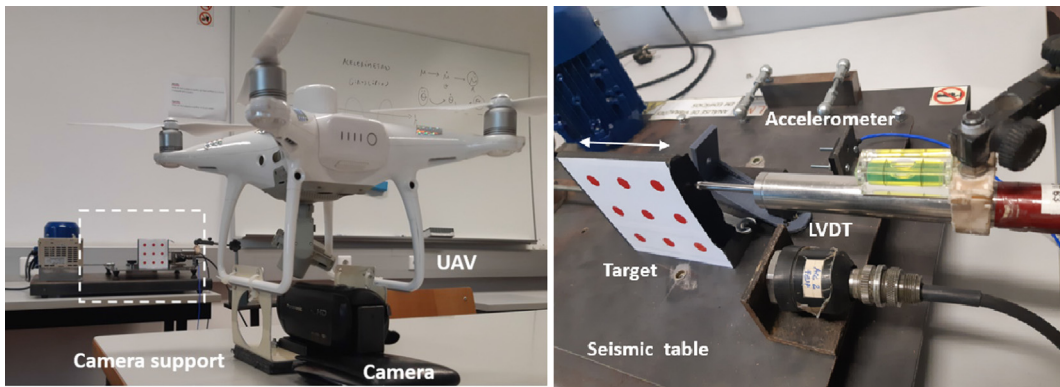


**Fig. 13.** Experimental layout of the laboratory test.

tion rate equal to 50 fps. The target and DC accelerometer were fixed to the seismic table. The seismic table is capable of simulating horizontal movements with frequencies varying between 0.1 Hz and 5.0 Hz and displacement amplitude limit equal to  $\pm 10$  mm.

The contact measurement system involved the installation of a LVDT, RDP model ACT1000A, which was supported on a tripod resting on the floor.

The signal acquisition of the accelerometer and the LVDT was carried out using a portable data acquisition system, NI cDAQ USB-9162, and through a 24-bit IEPE module. This system connects to a laptop through a USB protocol.



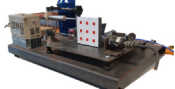


Table 1 shows the main components of the displacement measurement system for the laboratory test, including their main technical characteristics. The components of the video system were previously presented in Fig. 2.

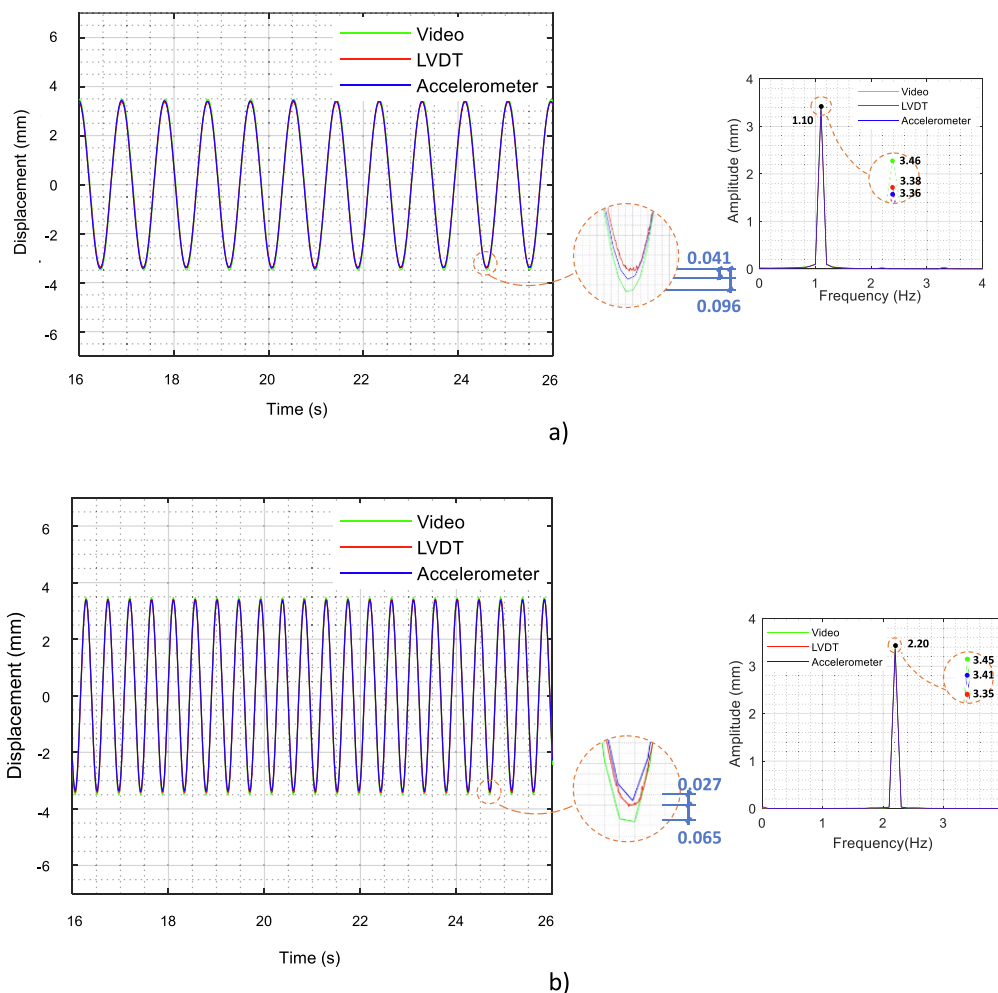
The objective of the laboratory test was to compare the displacement records obtained through the LVDT with: i) the displacement records obtained through the video system, in order to validate the video image processing tool, and ii) the displacement records obtained through the double integration of the DC accelerometer signal, in order to validate the numerical integration tool.

Fig. 14 shows the comparison of the displacement records obtained through the LVDT, the video system and the accelerometer (through the double integration of the accelerations), considering the frequencies of the movement of the seismic table equal to 1.10 Hz (Fig. 14a) and 2.20 Hz (Fig. 14b). The beginning and end parts of the records were removed due to the signal distortion effect resulting from the double integration of the acceleration records. Additionally, the amplitudes of the Fast Fourier Transforms (FFT) of each time-record are also presented in Fig. 14c and d.

Overall, there is an excellent agreement between the displacement records obtained through the LVDT, the video camera and the double integration of the DC accelerometer signal, regarding both the time and frequency domains. In terms the time domain, the greatest difference between the peak values of the video system and the LVDT is equal to 0.096 mm (3.10% relative error) for the vibration frequency of 1.10 Hz, which is lower than the resolution of digital images, equal to 0.145 mm/pixel. The most significant difference between the peak values of the displacements obtained through the accelerometer (double integration) and the LVDT was 0.041 mm (1.79% relative error), also for the 1.10 Hz vibration frequency.

**Table 1**  
Complementary equipment for the laboratory test.

Component	Brand/model		Technical characteristics
LVDT	RDP/ACT1000A		Measurement range: $\pm 50$ mm Linearity error (%F.S.): $\pm 0.5$ Sensitivity: 1.5 V/V Mass: 320 g
Differential MEMS DC Accelerometer	PCB/3741B1210G		Measurement range: $\pm 10$ g Broadband Resolution: 1.2 mg rms Sensitivity: 200 mV/g
Vibration Table			Frequency range: 0 Hz–1000 Hz Frequency range: 0.1 Hz–5.0 Hz Amplitude: $\pm 3.4$ mm
Data Acquisition System	NI/cDAQ USB-9162		Bus interface: USB 2.0 Hi-Speed 1-Slot
IEPE module	NI-9234		Number of channels: 4 Resolution: 24-bits Max. sample rate: 51.2 kS/s/ch Noise at maximum sample rate: 50 $\mu$ Vrms



**Fig. 14.** Comparison of the displacement records of the LVDT, the video system and the accelerometer (through the double integration of the accelerations), and corresponding FFT amplitudes, considering the frequencies of the movement of the seismic table to be: a) 1.10 Hz, b) 2.20 Hz.



In the frequency domain, the excitation frequencies were similarly estimated by all sensors, and the peak values have a maximum relative difference equal to 2.98% between the video and LVDT, for the vibration frequency of 2.20 Hz. Additionally, the maximum FFT phase shifts, taking as reference the LVDT record, are equal to  $0.27^\circ/0.31^\circ$  for the accelerometer, and  $8.80^\circ/11.51^\circ$  for the video, respectively for excitation frequencies of 1.10 Hz and 2.20 Hz.

#### 4.2. Field test

The field test consisted of measuring the displacements of a target fixed to a massive Reinforced Concrete (RC) wall based on the video system and with the UAV in motion. In these circumstances, the target does not move, thus, according to Equation (1):

$$0 = \vec{\delta}_V^{Y,i} + \vec{\delta}_{UAV}^{Y,i} \quad (19)$$

Therefore, the virtual displacement of the target estimated by the video system is only due to the movements of the UAV (with opposite direction):

$$\vec{\delta}_V^{Y,i} = -\vec{\delta}_{UAV}^{Y,i} \quad (20)$$

The purpose of the test is to validate the inertial system of the UAV, particularly the numerical integration tool, by comparing the displacements obtained through the inertial and video systems. If the inertial system works properly, both displacements values tend to be equal unless the sign. Therefore, in future applications, it will be possible to subtract the displacements of the UAV from the displacements estimated by the video system.

Fig. 15 shows some details of the field test, namely the location of the target fixed to the wall, the UAV with the on-board video system and the local RTK station. The operational distance of the UAV from the target varied between 4.70 m and 5.20 m. The RTK positioning system allowed reducing the range of movements of the UAV due to the drag force of the wind.

The main constraint to carrying out the test was related to the limited autonomy of the UAV batteries due to the increased weight of the external camera and the permanent connection to the RTK. This fact conditioned the duration of the flights to time periods not exceeding 3 min. The flight time includes the take-off, the UAV positioning close to the target, the measurement and landing. The test was carried out in light wind conditions and without significant variation in the brightness of the camera's field of vision.

Fig. 16a shows the records of the horizontal displacements of the target obtained through the video system and the inertial system (with opposite sign) based on a flight measurement period lasting 1 min 24 s (84 s). Fig. 16b and c present the



Fig. 15. Experimental layout of the field test.

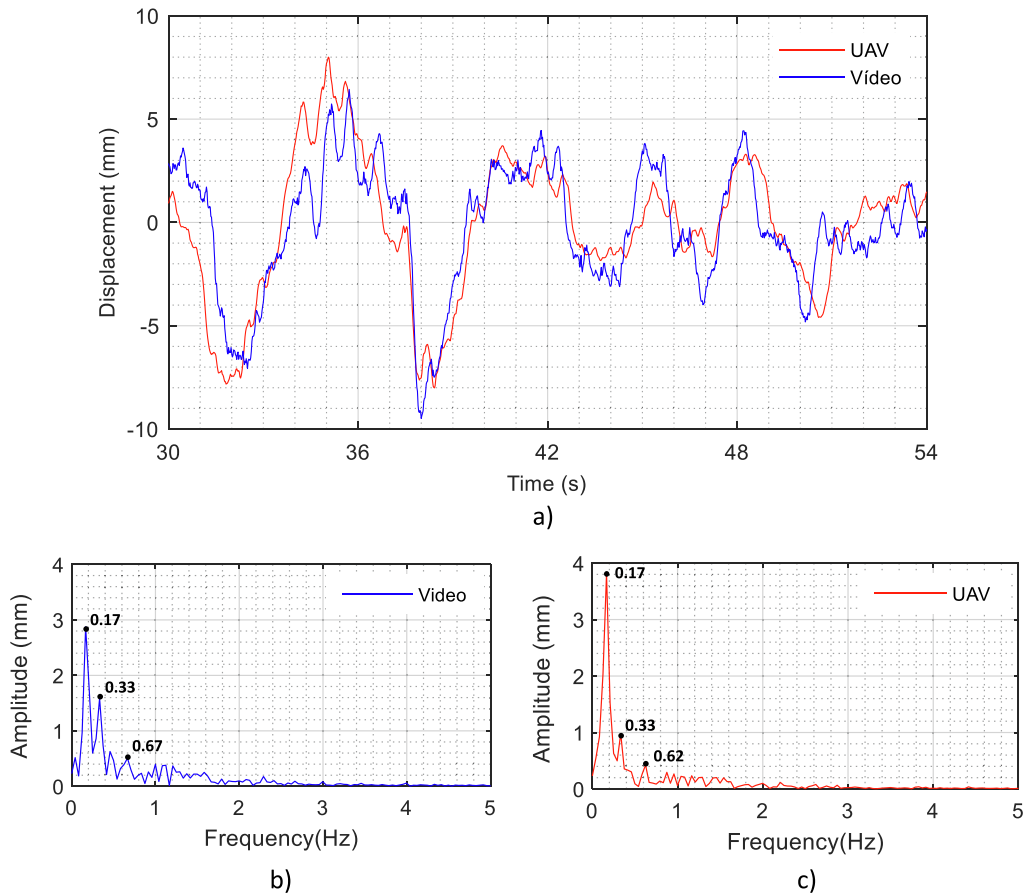


**Fig. 16.** Comparison of displacement records obtained through the video system and the UAV inertial system, and corresponding FFT amplitudes.

**Table 2**

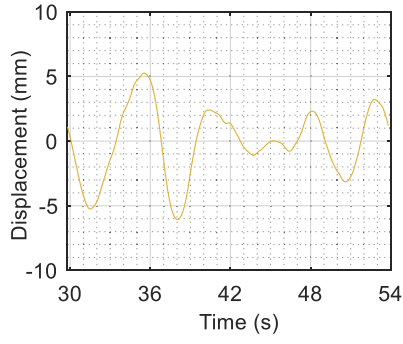
Measurement accuracy of different vision-based displacement systems mounted on UAVs.

Author	Year	Location	Weather conditions	Measurement accuracy	
				Peak value	RMS
Ellenberg et al. [21]	2015	Indoor	No wind and good light conditions	–	5.12%
Yoon et al. [23]	2018	Indoor	No wind and good light conditions	–	2.14 mm
Zhang et al. [15]	2019	Indoor	No wind and very good light conditions	–	2.90 mm
Garg et al. [24]	2019	Outdoor	Light wind and different light conditions at sunset	5%	10%
Present study	2020	Outdoor	Light wind and good light conditions	15.5% (1.47 mm)	9.3% (2.02 mm)

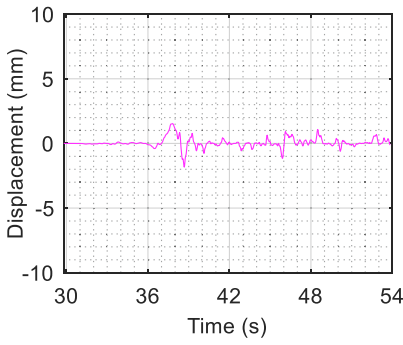
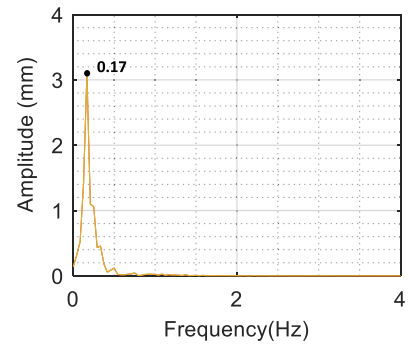
corresponding FFT amplitudes. The initial ([0–30]s) and final ([54–84]s) parts of the records were removed because of the distortion effect of the signal resulting from the double integration of the acceleration records.

The displacements of the UAV were estimated by applying the mathematical formulation presented in Section 2.3, in particular the Expression (10). For this purpose, a focal distance of 10.30 mm was considered, corresponding to the use of a 5× optical zoom, a distance from the IMU to the video camera sensor equal to 217 mm, and an image resolution ranging from 1.52 px/mm to 1.69 px/mm, depending on the operational distance between the UAV and the target. The numerical integration of the acceleration and angular velocity records used a high-pass FIR- Kaiser filter with a cutoff frequency equal to 0.10 Hz. In turn, the displacements of the video system were estimated according to the indications in Section 3.1. The synchronization of the displacement records was carried out based on the previous adjustment of the camera and UAV clocks according to the time of the RTK system.

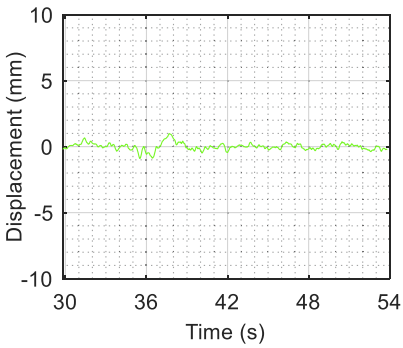
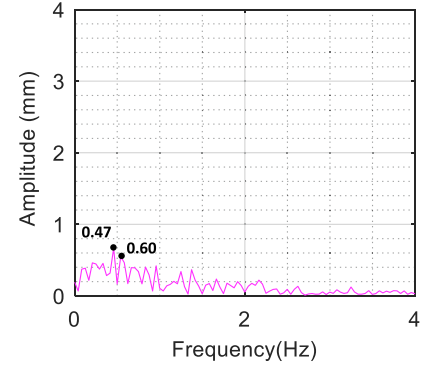
Overall, Fig. 16a shows a good agreement between the displacement records obtained by the video system and the UAV inertial system. In some time intervals, such as between 37 s and 43 s, the agreement is actually very good. The relative error between the mean square values (RMS) of the records is equal to +9.3% using the video system as a reference. In turn, the



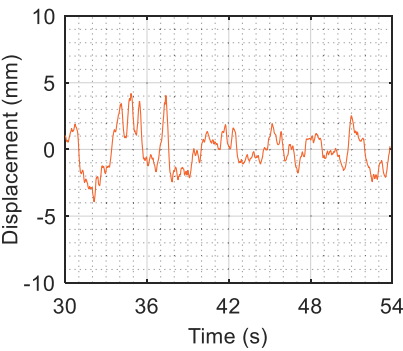
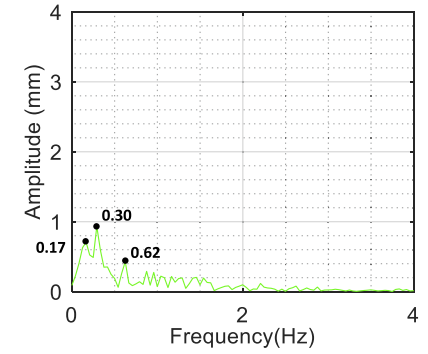
a)



b)



c)



d)

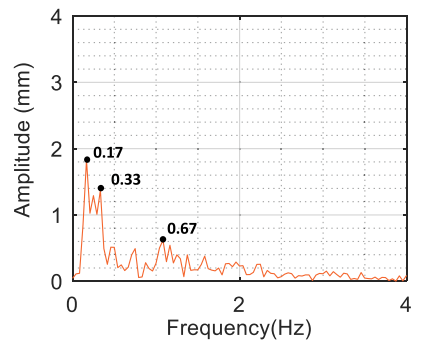


**Fig. 17.** Time-records of the horizontal displacements of the target, and corresponding FFT amplitudes, obtained through the inertial system, associated to each of the UAV movement terms: a)  $\delta_y^{y,i}$ , b)  $\delta_x^{y,i}$ , c)  $\delta_x^{y,i}$ , d)  $\delta_y^{y,i}$

difference between the peak values of both records is equal to  $-1.47$  mm, which corresponds to a relative error of  $-15.5\%$ , taking the results of the video system as reference. Table 2 compares the performance of the developed vision-based displacement system with other systems refereed in the bibliography, in terms of peak value and RMS measurement errors, as well as the observable wind and lighting conditions. The measurement errors obtained in the present study are in the same order of magnitude of those observed in the existing bibliography. In most situations, the experimental tests reported in the bibliography were performed indoor under ideal environmental conditions, i.e., no wind and good/very good lighting conditions.

Regarding the auto-spectra, it is possible to see in both records that the highest amplitude peaks occur for frequencies equal to  $0.17$  Hz,  $0.33$  Hz and  $0.62/0.67$  Hz, and are predictably related to movements of the UAV induced by the wind. It is also observed that there are UAV movements associated with frequencies above  $0.50$  Hz, although less significant. It should be noted that the frequency value equal to  $0.50$  Hz was taken as a truncation limit by several authors [2,24] to eliminate from the displacement records the contributions associated with the movements of the UAV.

Fig. 17 shows the time-records of the horizontal displacements of the target, and corresponding FFT amplitudes, obtained through the inertial system, associated with each of the terms of the UAV movement that induce virtual displacements of the target in the direction Y, in particular, the term due to the movement in the direction Y ( $\delta_Y^{Y,i}$ ) (Fig. 17a), the term due to the movement in the direction X ( $\delta_X^{Y,i}$ ) (Fig. 17b), the term due to the rotation around axis X ( $\delta_X^{Y,i}$ ) (Fig. 17c) and the term due to the rotation around axis Z ( $\delta_Y^{Y,i}$ ) (Fig. 17d).

The results show that the terms that most influence the values of the horizontal displacement of the target are those related to the movement of the UAV in the direction Y and those related to its rotation around axis Z. The term resulting from the movement of the UAV in the direction Y is characterized by a very low frequency movement induced by the wind. The term of the UAV movement related to its rotation around axis Z, in addition to being influenced by very low frequencies, is also influenced by slightly higher frequencies, in the range between  $0.5$  Hz and  $1.5$  Hz. Some of these frequencies are possibly related to movements induced by the UAV control unit for positioning corrections, and by the UAV operator that is remotely controlling the flight.

## 5. Conclusions and future developments

This article describes a methodology for estimating in-plane horizontal displacements of Civil Engineering structures based on data collected from a UAV on-board video system in conjunction with an embedded IMU. The proposed methodology relies, first, on the calculation of the relative displacements of the UAV-structure based on precision target tracking, and second, on the UAV motion subtraction based on the data derived from the IMU, in order to estimate the absolute structural displacement. In this way the response of the structure is independent from the response of the UAV, including situations where the movements of the structure and UAV are in phase.

The image processing techniques are based on heuristic features, particularly on segmentation, while the IMU data processing, specifically the data from the DC accelerometer and gyroscopes, relies on the application of an efficient numerical integration strategy.

The success of the integration process requires a baseline correction of the records, performed by high-pass digital filters, and a rigorous control of the distortion errors that occur at the beginning and end parts of the records. Consequently, a reliable strategy for estimating absolute displacements will require longer measurement periods because, for very low cutoff frequencies, the affected parts of the records may assume significant time values. For example, using a cutoff frequency equal to  $0.10$  Hz causes a distortion of the displacement record over  $60$  s.

The validation of the proposed methodology was based on exploratory dynamic tests performed in the laboratory and in the field. The laboratory test involved measuring the displacements of a moving target, positioned over a seismic table, by means of a LVDT, a DC type accelerometer and the UAV video system in stationary position. An excellent agreement was achieved for the three displacement estimates, both in frequency and amplitude, as evidenced by the highest difference observed in the values. That occurred between the video system and the LVDT and was equal to  $0.096$  mm for the case of a  $1.10$  Hz excitation frequency, which is lower than the resolution of digital images, equal to  $0.145$  mm/px.

The field test consisted of measuring the displacements of a target fixed to a wall considering the non-stationary UAV video system. Under these circumstances, with no movements of the target, the virtual displacement of the target estimated by the video system is exclusively due to the self-movements of the UAV. The comparison between the video and IMU displacement records shows a good agreement, with a peak value error of  $1.47$  mm ( $15.5\%$  relative error) and a RMS error of  $9.3\%$ . These errors can be eventually justified by the occurrence of small relative displacements between the UAV and the external video system, due, to some extent, to the flexible connection between these two components. In any case, the accuracy of the results is in the same order of magnitude of those observed in the existing bibliography, which, in most situations, were performed in indoor conditions with no wind and good/very good lighting conditions. Additionally, this test allowed to understand which specific degrees-of-freedom of the UAV are more prone to affect the performance of the measurement system due to the influence of wind actions, typically for frequencies below  $0.50$  Hz, and the manual/automatic remote control of the UAV, at frequencies between  $0.50$  Hz and  $1.5$  Hz.

For future studies, the authors intend to upgrade the proposed methodology for a non-target displacement evaluation system based on Digital Image Correlation techniques, which will be particularly useful for structures with limited accessi-

bility. Additionally, some specific field applications will be carried out to evaluate the displacements of a metallic railway bridge under traffic actions [7,38] and a telecommunications tower under wind actions [5]. This second case involves a high-rise flexible structure with the main natural frequencies in the range 0.40–0.80 Hz.

### CRediT authorship contribution statement

**D. Ribeiro:** Conceptualization, Methodology, Validation, Investigation, Writing - original draft, Writing - review & editing, Supervision, Funding acquisition. **R. Santos:** Conceptualization, Methodology, Validation, Investigation. **R. Cabral:** Methodology, Software, Validation, Investigation, Writing - original draft, Writing - review & editing. **G. Saramago:** Software, Validation, Investigation, Writing - original draft. **P. Montenegro:** Software, Validation, Investigation. **H. Carvalho:** Software, Validation, Investigation. **J. Correia:** Validation, Investigation. **R. Calçada:** Investigation, Resources, Supervision, Funding acquisition.

### Declaration of Competing Interest

The authors declare that they have no known competing financial interests or personal relationships that could have appeared to influence the work reported in this paper.

### Acknowledgements

The authors would like to thank HP Drones, in particular Mr. Hanniel Pontes, for the loan of equipment to carry out the campaigns, Professors Jorge Justo and Fernando Ferreira, from the Department of Mechanical Engineering of ISEP, for the availability of the equipment of the Laboratory of Applied Mechanics, and the Base Funding – UIDB/04708/2020 of the CONSTRUCT – Instituto de I&D em Estruturas e Construções – financed by national funds through the FCT/MCTES (PIDDAC).

### References

- [1] A.D. Orcesi, D.M. Frangopol, S. Kim, Optimization of bridge maintenance strategies based on multiple limit states and monitoring, *Eng. Struct.* 32 (3) (2010) 627–640.
- [2] V. Hoskere, J.-W. Park, H. Yoon, B.F. Spencer, Vision-based modal survey of civil infrastructure using unmanned aerial vehicles, *J. Struct. Eng.* 145 (7) (2019) 04019062, [https://doi.org/10.1061/\(ASCE\)ST.1943-541X.0002321](https://doi.org/10.1061/(ASCE)ST.1943-541X.0002321).
- [3] J. Song, C. Gu, H. Su, H. Gu, X. Huang, Observed displacement data-based identification method of structural damage in concrete dam, *Eng. Fail. Anal.* 66 (2016) 202–211.
- [4] F. Moreu, J. Li, H. Jo, R.E. Kim, S. Scola, B.F. Spencer, J.M. LaFave, Reference-free displacements for condition assessment of timber railroad bridges, *J. Bridge Eng.* 21 (2) (2016) 04015052, [https://doi.org/10.1061/\(ASCE\)BE.1943-5592.0000805](https://doi.org/10.1061/(ASCE)BE.1943-5592.0000805).
- [5] D. Ribeiro, J. Leite, N. Pinto, R. Calçada, Continuous monitoring of the dynamic behaviour of a high-rise telecommunications tower, *Struct. Design Tall Spec. Build.* 28 (11) (2019) e1621.
- [6] J. Malveiro, D. Ribeiro, R. Calçada, R. Delgado, Updating and validation of the dynamic model of a railway viaduct with precast deck, *Struct. Infrastruct. Eng.* 10 (11) (2014) 1484–1509.
- [7] D. Ribeiro, R. Calçada, J. Ferreira, T. Martins, Non-contact measurement of the dynamic displacement of railway bridges using an advanced video-based system, *Eng. Struct.* 75 (2014) 164–180.
- [8] J. Lee, K.-C. Lee, S. Jeong, Y.-J. Lee, S.-H. Sim, Long-term displacement measurement of full-scale bridges using camera ego-motion compensation, *Mech. Syst. Sig. Process.* 140 (2020) 106651, <https://doi.org/10.1016/j.ymssp.2020.106651>.
- [9] H.H. Nassif, M. Gindy, J. Davis, Comparison of laser Doppler vibrometer with contact sensors for monitoring bridge deflection and vibration, *NDT & E Int.* 38 (3) (2005) 213–218.
- [10] G. Luzzi, M. Crosetto, M. Cuevas-González, A radar-based monitoring of the collserola tower (Barcelona), *Mech. Syst. Sig. Process.* 49 (1–2) (2014) 234–248.
- [11] H.S. Park, H.M. Lee, H. Adeli, I. Lee, A new approach for health monitoring of structures: terrestrial laser scanning, *Comput.-Aided Civ. Infrastruct. Eng.* 22 (1) (2007) 19–30.
- [12] G.A. Stephen, J.M.W. Brownjohn, C.A. Taylor, Measurements of static and dynamic displacement from visual monitoring of the Humber Bridge, *Eng. Struct.* 15 (3) (1993) 197–208.
- [13] D. Lydon, M. Lydon, S.u. Taylor, J.M. Del Rincon, D. Hester, J. Brownjohn, Development and field testing of a vision-based displacement system using a low-cost wireless action camera, *Mech. Syst. Sig. Process.* 121 (2019) 343–358.
- [14] R. Jiang, D.V. Jáuregui, K.R. White, Close-range photogrammetry applications in bridge measurement: literature review, *Measurement* 41 (8) (2008) 823–834.
- [15] X. Zhang, Y. Zeinali, B.A. Story, D. Rajan, Measurement of three-dimensional structural displacement using a hybrid inertial vision-based system, *Sensors* 19 (19) (2019) 4083, <https://doi.org/10.3390/s19194083>.
- [16] C.-Z. Dong, O. Celik, F.N. Catbas, E.J. O'Brien, S.u. Taylor, Structural displacement monitoring using deep learning-based full field optical flow methods, *Struct. Infrastruct. Eng.* 16 (1) (2020) 51–71.
- [17] C.-Z. Dong, F.N. Catbas, A non-target structural displacement measurement method using advanced feature matching strategy, *Adv. Struct. Eng.* 22 (16) (2019) 3461–3472.
- [18] S. Bhowmick, S. Nagarajaiah, Z. Lai, Measurement of full-field displacement time history of a vibrating continuous edge from video, *Mech. Syst. Sig. Process.* 144 (2020) 106847, <https://doi.org/10.1016/j.ymssp.2020.106847>.
- [19] D. Ribeiro, R. Santos, A. Shibasaki, P. Montenegro, H. Carvalho, R. Calçada, Remote inspection of RC structures using unmanned aerial vehicles and heuristic image processing, *Eng. Fail. Anal.* 117 (2020) 104813, <https://doi.org/10.1016/j.engfailanal.2020.104813>.
- [20] H. Yoon, H. Elanwar, H. Choi, M. Golparvar-Fard, B.F. Spencer, Target-free approach for vision-based structural system identification using consumer-grade cameras, *Struct. Control Health Monit.* 23 (12) (2016) 1405–1416.
- [21] A. Ellenberg, L. Branco, A. Krick, I. Bartoli, A. Kontsos, Use of unmanned aerial vehicle for quantitative infrastructure evaluation, *J. Infrastruct. Syst.* 21 (3) (2015) 04014054, [https://doi.org/10.1061/\(ASCE\)IS.1943-555X.0000246](https://doi.org/10.1061/(ASCE)IS.1943-555X.0000246).
- [22] H. Yoon, V. Hoskere, J.-W. Park, B. Spencer, Cross-correlation-based structural system identification using unmanned aerial vehicles, *Sensors* 17 (9) (2017) 2075, <https://doi.org/10.3390/s17092075>.



- [23] H. Yoon, J. Shin, B.F. Spencer, Structural displacement measurement using an unmanned aerial system, *Comput.-Aided Civ. Infrastruct. Eng.* 33 (3) (2018) 183–192.
- [24] P. Garg, F. Moreu, A. Ozdagli, M.R. Taha, D. Mascareñas, Noncontact dynamic displacement measurement of structures using a moving laser doppler vibrometer, *J. Bridge Eng.* 24 (9) (2019) 04019089, [https://doi.org/10.1061/\(ASCE\)BE.1943-5592.0001472](https://doi.org/10.1061/(ASCE)BE.1943-5592.0001472).
- [25] R. Herrmann, A. Moortgat-Pick, S. Marx, Vibration analysis of structures using a drone (UAV) based mobile sensing platform, in: *Proceedings of 5th International Conference on Smart Monitoring, Assessment and Rehabilitation of Civil Structures*, 2019, Potsdam, Germany.
- [26] P. Liu, A.Y. Chen, Y.-N. Huang, J.-Y. Han, J.-S. Lai, S.-C. Kang, T.-H. Wu, M.-C. Wen, M.-H. Tsai, A review of rotorcraft Unmanned Aerial Vehicle (UAV) developments and applications in civil engineering, *Smart Struct. Syst.* 13 (6) (2014) 1065–1094.
- [27] H. Shakhatareh, A. Sawalmeh, A. Al-Fuqaha, Z. Dou, E. Almaita, I. Khalil, N. Othman, A. Khreishah, M. Guizani, Unmanned aerial vehicles: a survey on civil applications and key research challenges, *IEEE Access* 7 (2019) 48572–48634.
- [28] C. Abellanos, R. Lugpatan, D. Pascua, Position estimation using inertial measurement unit (IMU) on a quadcopter in an enclosed environment, *Int. J. Comput. Commun. Instrum. Eng.* 3(2) (2016) 2349–1477.
- [29] S. Rocha, J. Feiteira, P. Mendes, U. Da Silva, R. Pereira, Method to measure displacement and velocity from acceleration signals, *J. Eng. Res. Appl.* 6 (6–4) (2016) 52–59.
- [30] H. Sekiya, K. Kimura, C. Miki, Technique for determining bridge displacement response using MEMS accelerometers, *Sensors* 16 (2) (2016) 257, <https://doi.org/10.3390/s16020257>.
- [31] Y. Yang, Y. Zhao, D. Kang, Integration on acceleration signals by adjusting with envelopes, *J. Meas. Eng.* 4 (2) (2016) 117–121.
- [32] D. Arias-Lara, J. De-la-Colina, Assessment of methodologies to estimate displacements from measured acceleration records, *Measurement* 114 (2018) 261–273.
- [33] Q. Yang, L. Sun, A fuzzy complementary Kalman filter based on visual and IMU data for UAV landing, *Optik* 173 (2018) 279–291.
- [34] C. Zheng, Z. Liu, T. Wu, H. Wang, Y. Wu, X. Shi, Experimental investigation of vortex-induced vibration of a thousand-meter-scale mega-tall building, *J. Fluids Struct.* 85 (2019) 94–109.
- [35] Panasonic Corporation. Basic Owner's Manual High-Definition Video Camera: Model No. HC-W580 HC-V380. 2015. Newark, USA.
- [36] C. Ricolfe-Viala, A.-J. Sanchez-Salmeron, Lens distortion models evaluation, *Appl. Opt.* 49 (30) (2010) 5914–5928.
- [37] B. Pan, L. Yu, D. Wu, L. Tang, Systematic errors in two-dimensional digital image correlation due to lens distortion, *Opt. Lasers Eng.* 51 (2) (2013) 140–147.
- [38] D. Ribeiro, R. Calçada, R. Delgado, M. Brehm, V. Zabel, Finite element model updating of a bowstring-arch railway bridge based on experimental modal parameters, *Eng. Struct.* 40 (2012) 413–435.